Induced polarization as a tool to non-intrusively characterize embankment hydraulic properties

A Soueid Ahmed, A Revil, F Abdulsamad, B Steck, C Vergniault, V Guihard

Engineering Geology 271 (2020) 105604

Contents lists available at ScienceDirect

Engineering Geology

journal homepage: www.elsevier.com/locate/enggeo

Induced polarization as a tool to non-intrusively characterize embankment hydraulic properties

A. Soueid Ahmed[a], A. Revil[a,*], F. Abdulsamad[a], B. Steck[b], C. Vergniault[c], V. Guihard[b]

[a] USMB, CNRS, EDYTEM, Université Grenoble Alpes, 73000 Chambéry, France
[b] EDF R&D, 6 quai Watier, 78400 Chatou, France
[c] EDF DI-TEGG, 905 avenue du Camp de Menthe, 13097 Aix-en-Provence, France

ARTICLE INFO

Keywords:
Induced polarization
Electrical properties
Permeability
Earth dam
Petrophysics

ABSTRACT

Characterizing key petrophysical parameters of dams and embankments (including water content, specific surface area or cation exchange exchange capacity, and permeability) is an important task in estimating their degree of safety. So far, induced polarization tomography has not been investigated to check if it can play such a role. We have conducted a time domain induced polarization profile along the embankment of a canal in the South East of France. The profile is 560 *m* long. It comprises 1696 apparent resistivity and chargeability data and was accomplished by separating the current and voltage electrode cables to improve the signal-to-noise ratio. In order to complement the study, we performed induced polarization measurements on six core samples (including a clayey material and five carbonate rocks) collected from outcrops. A petrophysical induced polarization model called the dynamic Stern layer model is tested to see how the electrical conductivity and the normalized chargeability can be both connected to the porosity, the cation exchange capacity (CEC), and permeability of these materials. Then, these results are applied to interpret the electrical conductivity and normalized chargeability tomograms into water content and CEC tomograms. In turn, these two parameters are used to compute a permeability index.

1. Introduction

Earth dams and embankments play an important role in water resources management and flood remediation. These infrastructures need continuous maintenance and meticulous monitoring in order to detect as soon as possible any anomaly that may affect their integrity (e.g., Fell et al., 1992, 2003; Lee et al., 2005). In this context, knowing the materials property distribution of these infrastructures provides valuable information to monitor their safety. Geophysical investigations, especially geoelectrical methods, offer the possibility of non-intrusively imaging of Earth dams and embankments (e.g., Panthulu et al., 2001). In this context, the self-potential (Rozycki et al., 2006; Soueid Ahmed et al., 2019), electrical resistivity (Fransisco et al., 2018; Himi et al., 2018) and mise-à-la masse methods (Ling et al., 2019) have played a great role in localizing leakages in dams and embankments.

Induced polarization is a non-intrusive sensing technique used to investigate the low-frequency (< 100 Hz) polarization mechanisms occurring in porous media after being exposed to a primary current or electrical field (e.g., Lesmes and Frye, 2001). By polarization, we mean here the reversible storage of electrical charges in porous media through mechanisms that are non-dielectric in nature (see Revil, 2013a, 2013b). The induced polarization method was first described by Schlumberger (1920) but its use was, for a long time, restricted to mineral exploration for reasons related to the high signal-to-noise ratio of induced polarization for such applications (e.g., Bleil, 1953; Pelton et al., 1978; Zonge and Wynn, 1975). In the last decades, induced polarization has been increasingly used in the realm of environmental engineering because of the development of more sensitive equipments and better metrological developments to improve the signal-to-noise ratio of the method (e.g., Börner et al., 1996; Slater and Lesmes, 2002; Kemna et al., 2012; Weller et al., 2013). In addition, such developments have benefited from a better understanding of the physics of the underlying polarization mechanisms in porous materials (e.g., Rosen et al., 1993; Revil and Florsch, 2010; Revil, 2012; Revil, 2013a, 2013b). Furthermore, induced polarization can be used to predict, to some extents, the permeability of porous media (Scott and Barker, 2003; Weller et al., 2010) and may therefore be useful to characterize dams and embankments hydraulic properties.

* Corresponding author.
E-mail addresses: abdellahi.soueid-ahmed@univ-smb.fr (A. Soueid Ahmed), andre.revil@univ-smb.fr (A. Revil), feras.abdulsamad@univ-smb.fr (F. Abdulsamad), barthelemy.steck@edf.fr (B. Steck), christophe.vergniault@edf.fr (C. Vergniault), vincent.guihard@edf.fr (V. Guihard).

https://doi.org/10.1016/j.enggeo.2020.105604
Received 1 January 2020; Received in revised form 19 March 2020; Accepted 20 March 2020
Available online 24 March 2020

In time domain induced polarization, a box (primary) current is injected in the ground for a period T using a pair of electrodes A and B (source and sink). The difference of electrical potential is measured using several bipoles of electrodes M and N. The secondary voltage on a bipole MN decays over time after the shut-down of the primary current. The existence of such a decay reflects that the ground behaves as a capacitor, storing reversibly electrical charges. The strength of this polarization is characterized by a physical parameter called the chargeability. For the frequency-domain induced polarization (often called spectral induced polarization), a complex electrical conductivity is measured with an in-phase component describing pure conduction phenomena and an imaginary or quadrature component reflecting pure polarization phenomena. The quadrature conductivity and the normalized chargeability (the product of the chargeability by the electrical in-phase conductivity) are proportional to each other. This relationship can be used to connect frequency and time-domain induced polarization (e.g., Revil et al., 2017a). In the field, time domain induced polarization measurements are favored due to the swiftness of their acquisition compared to spectral induced polarization measurements. In the laboratory, we usually prefer using spectral induced polarization but the relationship between the two approaches are pretty well-established (e.g., Kemna et al., 2012).

The main scientific question we want to tackle in the present study is to investigate the possibility of discriminating lithology and material properties (permeability, water content, cation exchange capacity) in earth dams and embankment structures using the induced polarization method. In this context, it is important to recall the limitation of the DC resistivity method alone, however, broadly used to characterize earth dams and embankments. Electrical conductivity depends on two contributions, a bulk conductivity (mostly dependent on the water content and salinity of the pore water) and a surface conductivity mostly controlled by the cation exchange capacity (CEC) of the material, which is proportional to its specific surface area. Electrical conductivity/resistivity cannot be used as a stand-alone technique to separate these two contributions. Induced polarization offers a remedy to this issue and can be used in concert with resistivity to separate the effect of the water content from the effect of the CEC when the salinity of the pore water is known or independently estimated. Abdulsamad et al. (2019) recently performed a first step in this direction. They worked with an experimental dam located at Aix-en-Provence (South of France). They used a controlled leakage area and showed that the induced polarization method is capable of imaging the changes in the water content associated with the leak.

In the present paper, we use the induced polarization method for characterizing the material properties of a portion of the embankment of a canal in the South-East France. We investigate to what extent the induced polarization method can be used to delineate the lithology and image different key petrophysical parameters of the embankment structure. To the best of our knowledge, this is the first attempt to infer such physical properties in such environments from induced polarization tomography. Independent petrophysical measurements are performed using 6 samples collected on the site to see if induced polarization can distinguish between different lithologies and they are connected to porosity, CEC, and permeability. In turn, we develop a permeability index that we test in the field.

2. Petrophysical model and experiments

2.1. Theory

As mentioned above, induced polarization refers to the reversible storage of electrical charges at grain scales in a porous medium under the influence of the electrical field. Such low frequency polarization is associated with the existence of an electrical double layer coating the surface of the grains (e.g. Phan et al., 2004, Fig. 1). This double layer is itself composed of an external layer called the diffuse layer and an internal layer called the Stern layer. We first summarize the results of a petrophysical polarization model called the dynamic Stern layer polarization model (see Revil, 2013b, for a theoretical development). We consider a metal-free porous material. We apply to this porous material an external (primary) harmonic electric field $\boldsymbol{E} = \boldsymbol{E}_0 \exp(+i\omega t)$, $\boldsymbol{E}_0$ ($V\ m^{-1}$) denotes the amplitude, ω denotes the pulsation frequency (in rad s^{-1}), and t (in s) is time. Under the action of this applied electrical field, the grains get polarized, which generates a secondary electrical field in the opposite direction of the primary electrical field. In this condition, the porous material can be characterized by a frequency-dependent complex conductivity σ^* entering Ohm's law,

$$\boldsymbol{J} = \sigma^* \boldsymbol{E}, \tag{1}$$

where $\boldsymbol{J}$ and $\boldsymbol{E}$ denote the current density (A m^{-2}) and the electrical field (V m^{-1}), respectively. The complex conductivity is given by (Revil et al., 2017a, 2017b)

$$\sigma^*(\omega) = \sigma_\infty - M_n \int_0^\infty \frac{h(\tau)}{1 + (i\omega\tau)^{1/2}} d\tau, \tag{2}$$

where ω is the angular frequency (rad s^{-1}), τ is a relaxation time (in s), and $h(\tau)$ denotes a probability density for the distribution of the relaxation times associated with charges accumulations at grain scales. In Eq. (2), the quantity M_n denotes the normalized chargeability (expressed in S m^{-1}) and is defined by $M_n \equiv \sigma_\infty - \sigma_0$ where σ_∞ and σ_0 (both in S m^{-1}) denote the instantaneous and DC (Direct Current) conductivity of the porous material, respectively. They also correspond to the high (typically above 100 Hz) and low (typically around 0.1 Hz) frequency value of the electrical conductivity. In time-domain induced polarization, the quantity σ_∞ corresponds to the conductivity just after the application of the external (primary) electrical field. In this situation, all the charge carriers are mobile (Fig. 1 and Revil et al., 2017a). The quantity σ_0 (S m^{-1}) defines the conductivity of the material for a long application of the electrical field corresponding to steady-state conditions.

According to the theoretical model developed by Revil (2013b) we have,

$$\sigma_\infty = \frac{{s_w}^n}{F}\sigma_w + \left(\frac{{s_w}^{n-1}}{F\phi}\right)\rho_g B\,\mathrm{CEC}, \tag{3}$$

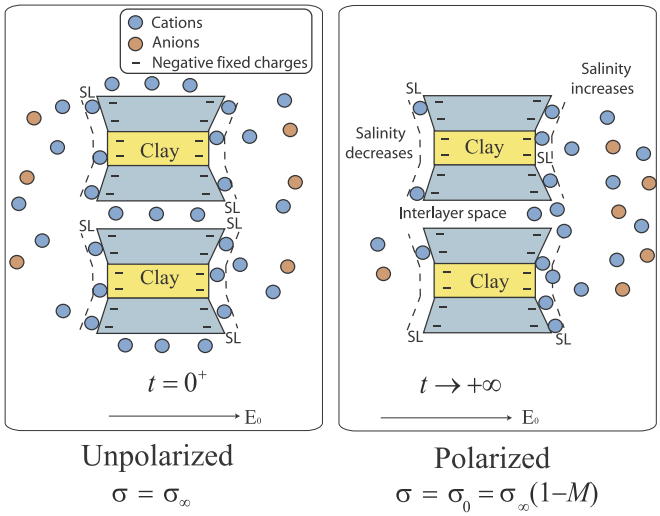

Fig. 1. Polarization of a clay grain under the effect of an applied electrical field. The polarization of the grain is responsible for a phase lag (between the electrical field and the current) in spectral induced polarization and a secondary voltage that can be observed after the (primary, applied) current is shut down in time-domain induced polarization.

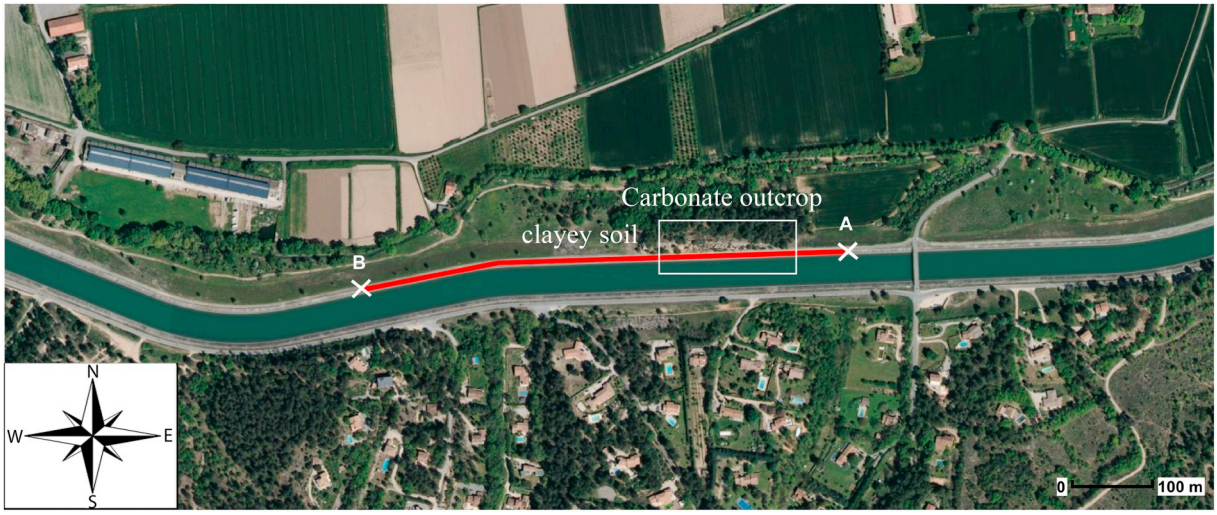

Fig. 2. Position of the geophysical profile along the embankment of the channel with the position of the carbonate outcrop and the clayey soil sample collected for the laboratory measurements.

$$\sigma_0 = \frac{{s_w}^n}{F}\sigma_w + \left(\frac{{s_w}^{n-1}}{F\phi}\right)\rho_g(B-\lambda)\mathrm{CEC}. \tag{4}$$

In these equations, F (dimensionless) denotes the intrinsic formation factor related to the porosity ϕ (dimensionless) by the first Archie's law $F = \phi^{-m}$ (generalized to $F = a\,\phi^{-m}$ for a collection of rock samples), m (dimensionless) is called the first Archie exponent or porosity exponent (Archie, 1942), n (dimensionless) is called the saturation exponent (dimensionless, generally $m \approx n$), s_w (dimensionless) denotes the water saturation related to the (volumetric) water content by $\theta = s_w\phi$, σ_w (in S m^{-1}) is the pore water conductivity, ρ_g denotes the grain density (in kg m^{-3}, usually $\rho_g = 2650$ kg m^{-3}), and CEC (C kg^{-1} where C stands for Coulomb) denotes the cation exchange capacity of the material. This CEC corresponds to the density of exchangeable surface sites on the surface of the mineral grains. It is typically measured using titration experiments in which the surface of the grains is exchanged with a cation having a high affinity for the sites populating the mineral surface. It is often expressed in meq/100 g with 1 meq/100 g = 963.20C kg^{-1}. In Eqs. (3) and (4), B (in $m^2s^{-1}\,V^{-1}$) denotes the apparent mobility of the counterions for surface conduction. By surface conduction, we mean the conductivity associated with conduction in the electrical double layer coating the surface of the grains. The quantity λ (in $m^2s^{-1}\,V^{-1}$) denotes the apparent mobility of the counterions for the polarization. The surface conductivity corresponds to the last term of Eq. (3) and is written as σ_S. A dimensionless number R has been introduced by Revil et al. (2017a) $R = \lambda/B$. From our previous studies (e.g., Ghorbani et al., 2018), we have $B(Na^+, 25\ ^\circ C) = 3.1 \pm 0.3 \times 10^{-9}\ m^2s^{-1}\ V^{-1}$ and $\lambda(Na^+, 25\ ^\circ C) = 3.0 \pm 0.7 \times 10^{-10}\ m^2s^{-1}\ V^{-1}$, and R is typically around 0.09 ± 0.01 (Ghorbani et al., 2018). Eqs. (3)–(4) together with the definition of the normalized chargeability leads to,

$$M_n = \left(\frac{{s_w}^{n-1}}{F\phi}\right)\rho_g\lambda\,\mathrm{CEC}. \tag{5}$$

The chargeability itself is a dimensionless quantity defined by $M = M_n/\sigma_\infty$.

In order to bridge time-domain and frequency-domain induced polarization, a quantitative relationship between the normalized chargeability and the quadrature conductivity is required. Considering the quadrature conductivity as the geometric mean of two frequencies f_1 and f_2 and the normalized chargeability defined as the difference between the in-phase conductivity at frequency $f_2 > f_1$ and the in-phase conductivity at the lower frequency f_1, we have (Van Voorhis et al., 1973)

$$\sigma''(\sqrt{f_1 f_2}) \approx -\frac{M_n(f_1,f_2)}{\alpha}, \tag{6}$$

$$\alpha \approx \frac{2}{\pi}\ln A, \tag{7}$$

where A corresponds to the number of decades separating f_1 and f_2. For instance for two decades $f_2 = 100f_1$, we have $A = 10^2$ and $\alpha \approx 3$. For 6 decades (which is typically the broader range of frequency of interest in induced polarization), we have $A = 10^6$ and $\alpha \approx 9$.

As discussed later in this paper, in the field we measure apparent resistivity and chargeability data on a set of electrodes. After being inverted, these provide tomographic images of the conductivity σ_∞ and normalized chargeability M_n distributions of the subsurface. This means that for each cell used to discretize the subsurface, we have two mapped parameters. Based on the previous petrophysical model and assuming $m = n$ (i.e., the cementation and saturation exponents are equal to each other, see justification in Revil, 2013a, 2013b, his fig. 18), we can determine the two unknowns of the problem, i.e. the water content and the cation exchange capacity (CEC) distributions (see Appendix A for details),

$$\theta = \left[\frac{1}{\sigma_w}\left(\sigma_\infty - \frac{M_n}{R}\right)\right]^{1/m}, \tag{8}$$

$$\mathrm{CEC} = \frac{M_n}{\theta^{m-1}\rho_g\lambda}, \tag{9}$$

where $\theta = s_w\phi$ denotes the water content and where m can be determined from petrophysical measurements as done in the next section (a value of $m = 2$ can be taken by default). Since λ, R, and ρ_g are all well-determined constants as discussed in the next section, Eqs. (8) and (9) require only the measurements of σ_∞ and M_n and the knowledge of m.

2.2. Laboratory experiments: procedures

The samples used in this study were collected at outcrops of the two formations visible at the ground surface of the test site discussed in Section 4 below (Figs. 2 and 3a). Sample #1 corresponds to a clayey soil. Samples #2 to #6 correspond to carbonate rock samples from a carbonate outcrops in the first section of the geophysical profile. The (connected) porosity was estimated from the volumes of the core samples and their dry and water-saturated weights. Their cation exchange capacity was estimated by the Hexamine cobalt chloride method and spectrophotometric titration (Ciesielski et al., 1997; Aran

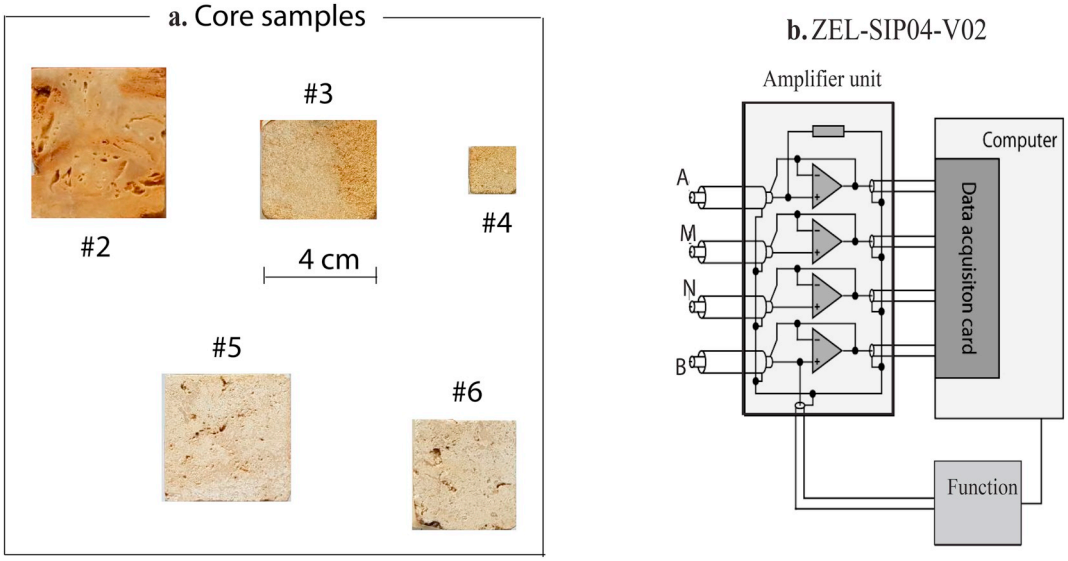

Fig. 3. Carbonate core samples used in this work from the test site and impedance meter used for the spectral induced polarization measurements. (a) We have 6 samples. The first sample (not shown here) is a clayey soil, which is unconsolidated. The five other samples are carbonate-rich rocks collected in the field at an outcrop at the beginning of the induced polarization profile. (b) Impedance meter ZEL/SIP04-V02 (Zimmermann et al., 2008).

et al., 2008). The complex conductivity experiments were made with the ZEL-SIP04-V02 impedance meter (Fig. 3b, see also Zimmermann et al., 2008). The spectra were obtained in the frequency range 0.01 Hz–45 kHz. They are reported in Fig. 4. The conductivity measurements are performed at three salinities: the in situ pore water conductivity using the water from the canal and two higher salinities using NaCl brines.

To estimate the surface conductivity σ_S and the formation factor F, we write Eqs. (3) or (4) as

$$\sigma = \frac{1}{F}\sigma_w + \sigma_S, \tag{10}$$

In order to avoid to give too much weight to the high salinity conductivity data, we fit the data as $X = \log_{10}(a10^Y + b)$ where $X = \log_{10}\sigma$, $Y = \log_{10}\sigma_w$ and the two model parameters are $a = 1/F$ and $b = \sigma_S$. The model parameters are obtained with a standard least square minimization technique. The fit of the curves is shown in Fig. 5. The porosity, CEC, formation factor, surface conductivity, normalized chargeability and quadrature conductivity are reported in Table 1.

2.3. Results

In Fig. 6, we plot the formation factor versus the porosity and we fit the trend with a generalized Archie's law $F = a\phi^{-m}$ where a and m are determined using a least square optimization procedure. In Fig. 7, we plot the surface conductivity and the normalized chargeability as a function of the reduced CEC defined as $\mathrm{CEC}/F\phi$ (see Eqs. (3) and (5)). The fit of the data provides the value of the mobilities B and λ. The good quality of the linear trends validates the theoretical predictions. Fig. 8 validates Eq. (6). According to Eq. (7), the coefficient α should be equal to 9, which is fairly close to the coefficient determined in Fig. 8 ($\alpha = 12 \pm 4$).

2.4. Permeability

The knowledge of the permeability distribution of an embankment is an essential ingredient to determine the potential for seepages. Sen et al. (1990) proposed the following relationship to determine the value of the permeability k (expressed in m^2) from the cation exchange capacity CEC (in C kg-1) and the porosity ϕ (dimensionless) thanks to the following semi-empirical equation,

$$k = k_0(1/FQ_V)^c, \tag{11}$$

where k_0 and c are two fitting parameters, $F \approx \phi^2$ and $Q_V = \rho_g(1-\phi)\mathrm{CEC}/\phi$ with ρ_g the grain density close to 2650 kg m^{-3}. The linear fit (least square regression) marked by the solid line in Fig. 9 yields $k \approx 10^{4.30}(1/FQ_V)^2$. Accounting for the dependence of the apparent formation factor and excess of charge per unit pore volume with the water content, Eq. (11) can easily be generalized to unsaturated conditions to

$$k \approx \frac{k_0\theta^6}{(\rho_g \mathrm{CEC})^2}, \tag{12}$$

with $k_0 = 10^{4.30}$ and k is expressed in m^2. From Eq. (12), it is clear that permeability in the vadose zone is extremely sensitive to the water content θ as expected. Along an embankment or in a dam, leakages would take permeable pathways that would be fully water-saturated. Therefore, we can determine a permeability index as

$$\mathfrak{I} \approx \frac{|\mathrm{Max}(\log_{10} k)|}{|\log_{10} k|}, \tag{13}$$

We will test this formula for the case study explored in the next section of this study.

3. Tomography: modeling procedure

In this section, we present and discuss time-domain induced polarization (TDIP) measurements and data inversion. This procedure will be applied to the field data in Section 4.

3.1. Macroscopic equations

TDIP measurements are favored in the field because they require less acquisition time and the current technology of resistivity meters allows induced polarization measurements to be performed simultaneously with resistivity measurements (Fig. 10). A TDIP experiment consists in injecting a current $I(t)$ (in A, t is time) between two electrodes A and B an then recording the voltage decay $\delta\psi_{MN}(t)$ between two potential electrodes M and N. Usually we prefer having the AB electrodes and the MN electrodes on two distinct cables to avoid electromagnetic (capacitive and inductive) coupling effects (Fig. 10). Once the primary current is shut down (for $t > 0$), only the secondary

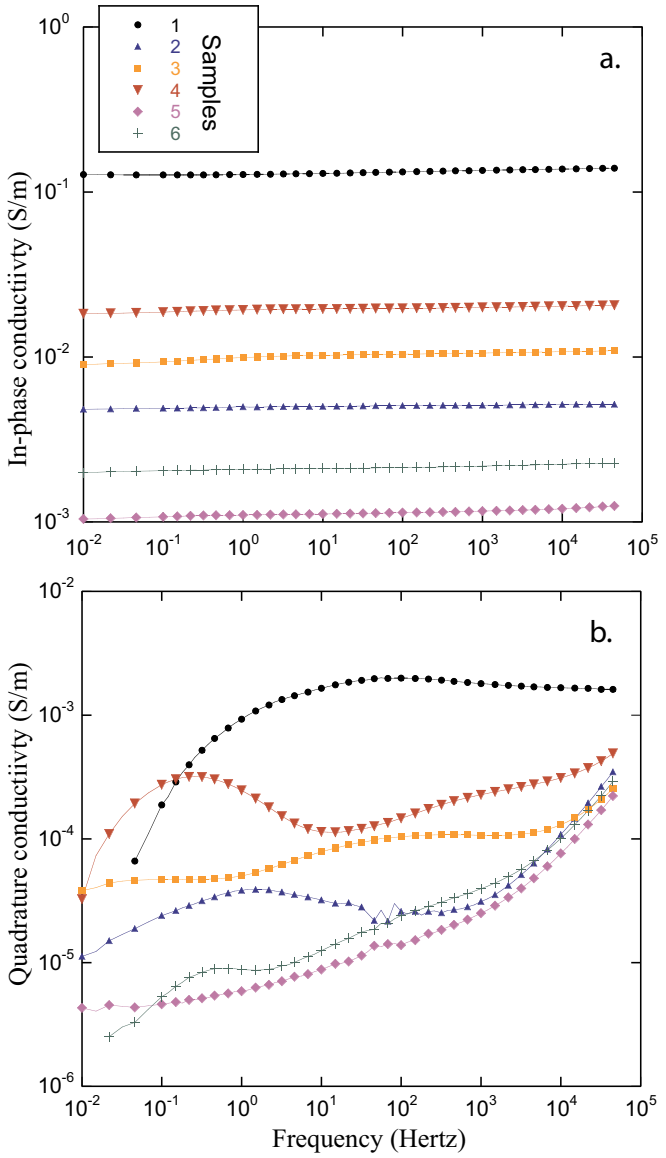

Fig. 4. Complex conductivity spectra of the 6 core samples considered in this work. (a) In-phase electrical conductivity spectra. (b) Quadrature conductivity spectra. The presence of several peaks can be associated to the existence of different peaks in the pore size distribution.

voltage persists. It is decaying over time while the charge carriers are coming back to their equilibrium position. This decaying secondary voltage is measured into windows (W_1, W_2, etc.) separated by characteristic times (t_0, t_1, t_2, …). The partial chargeabilities are determined for each of these windows by integrating the secondary voltage over time. T_{on} and T_{off} denote the time of current injection and time for potential decay measurement, respectively. The time t_0 is a delay (dead) time before starting the partial chargeability measurement.

The response of a 3D conductive medium to a given current excitation can be described by the following elliptic partial differential equation:

$$-\nabla\cdot(\sigma(x,y,z)\nabla\psi) = I\delta(x-x_s)(y-y_s)(z-z_s), \tag{14}$$

where $\sigma(x,y,z)$(in S m^{-1}) denotes the electrical conductivity distribution, ψ (in V) denotes the electrical potential generated by the injection of the current, δ is the Dirac distribution (used to simulate the injection of current at punctual sources or sinks A and B), x_s, y_s, and z_s are the spatial coordinates of the current sources or sink A and B. To solve Eq. (14), we need to specify the boundary conditions. We generally use the

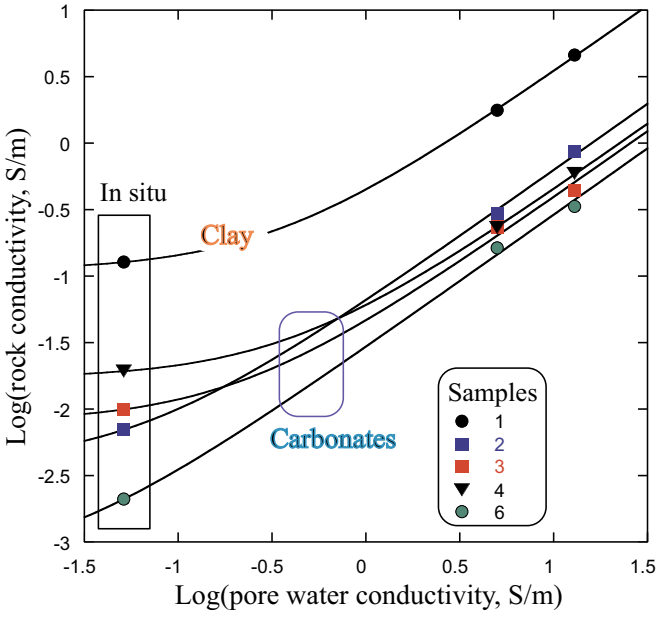

Fig. 5. Rock conductivity (at 1 Hz) versus pore water conductivity for some of the core samples used in this study. In situ represents the value of the in situ pore water conductivity in the canal along the embankment studied in the present paper. From these conductivity curves, we determine the formation factor and the surface conductivity in a log-log space using a non-linear fitting procedure based on a least-square technique. We also observe that at the in situ water conductivity, there is a strong effect of the surface conductivity.

following boundary conditions:

$$\psi = 0 \text{ on } \Gamma_D, \tag{15}$$

$$\sigma\nabla\psi\cdot\hat{n} = 0 \text{ on } \Gamma_N, \tag{16}$$

where Γ_D and Γ_N are known the Dirichlet's and Neumann's boundaries, respectively, $\Gamma_D \cup \Gamma_N = \Gamma$ (Γ represents all the boundaries of the domain), $\hat{n}$ is the outward unit vector that is normal to the boundary Γ_N. Physically, Eq. (16) means that when we get away from the area of current sources and sinks, the potential should drop to zero, while Eq. (16) refers to electric insulation and is applied at the top of our domain to simulate the ground/air interface. In the present paper, we will work on 2.5D induced polarization profiles. In this case, we still need to account for 3D effects and this could be achieved by simulating an infinite extension to the strike direction (i.e., the direction normal to the profile). We refer to this space as the 2.5 dimension. An efficient manner of solving Eq. (14) in 2.5D is obtained by solving it in the Fourier domain (e.g., Dey and Morrison, 1979):

$$-\nabla\cdot[\sigma(x,z)\nabla\tilde{\psi}(x,y,z)] + k^2\sigma(x,z)\tilde{\psi}(x,y,z) = \frac{I}{2}\delta(x-x_s)\delta(z-z_s) \tag{17}$$

where $\tilde{\psi}$ is the Fourier transform of ψ and k is the wavenumber. The potential is then obtained by:

$$\psi(x,y,z) = \frac{2}{\pi}\int_0^\infty \tilde{\psi}(x,k,z)\cos(ky)dk, \tag{18}$$

which numerically is computed through:

$$\psi = \sum_n \omega_n\tilde{\psi}(k_n) \tag{19}$$

where ω_n are weights that can be computed following the method reported in (Press et al., 1992). The macroscopic mechanisms of the TDIP problem can be described though the introduction of an intrinsic electrical property known as the chargeability M (i.e., Seigel, 1959). This parameter indicates the capacity of the medium of reversibly

Table 1
Material properties of the rock samples.

Sample	Porosity ϕ (−)	CEC (meq/100 g)	F (−)	σ_S (S m^{-1})	M_n (S m^{-1})	σ'' (S m^{-1})
1	0.30 ± 0.03	9.00	2.9	0.11	0.010163	165.0 × 10^{-5}
2	0.20 ± 0.03	0.97	16	0.0038	0.00032331	3.20 × 10^{-5}
3	0.20 ± 0.03	2.69	26	0.0080	0.0017825	7.86 × 10^{-5}
4	0.21 ± 0.03	3.58	23	0.017	0.0020288	11.4 × 10^{-5}
5	0.14 ± 0.03	0.32	63	0.00029	0.00016029	0.88 × 10^{-5}
6	0.17 ± 0.03	0.10	34	0.00060	0.00024974	1.25 × 10^{-5}

CEC denotes the cation exchange capacity (1 meq/100 g = 963.20C kg^{-1}), F denotes the formation factor (dimensionless), σ_S denotes the surface conductivity (S m^{-1}), M_n (S m^{-1}) the normalized chargeability (with the DC conditions taken at a low frequency of 0.01 Hz and the instantaneous conductivity taken at the high frequency of 10 kHz), and ϕ the connected porosity (dimensionless). The formation factor and the surface conductivity are determined using the rock conductivity versus the pore water conductivity in log log space. The quadrature conductivity is here provided at 10 Hz.

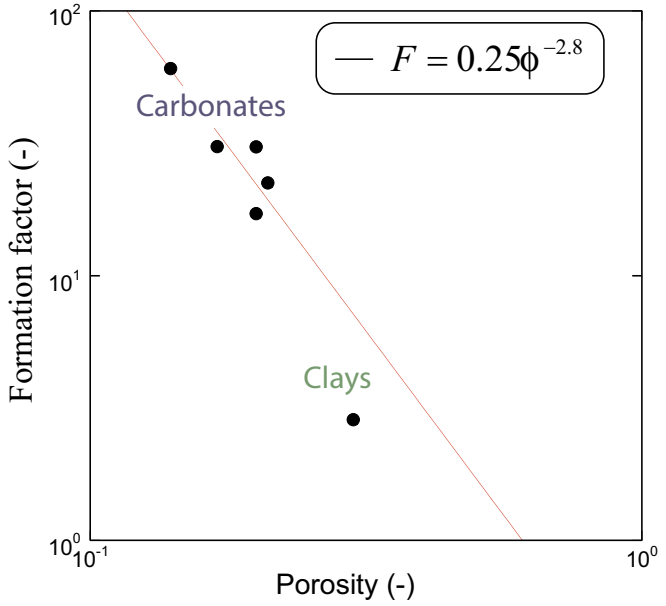

Fig. 6. Formation factor (dimensionless) versus (connected) porosity (dimensionless) and fit with an empirical Archie's law $F = a\phi^{-m}$ to determine the values of a and m.

storing electrical charges after been subject to a primary current. Seigel (1959) proposed to describe the polarization effects as a perturbation of the electrical conductivity. We can therefore compute a potential distribution that accounts for the polarization effects defined as:

$$\psi_\infty = G(\sigma_0(1 - M)) \tag{20}$$

where G is the operator associated to Eq. (14) in 3D and to Eq. (14) in 2.5D.

As reported in Oldenburg and Li (1994), the apparent chargeability can be computed as:

$$M_a = \frac{\psi_\infty - \psi_0}{\psi_\infty} \tag{21}$$

With $\psi_0 = G(\sigma_0)$. Eq. (21) means that in order to compute the induced polarization response we only need to solve Eq. (17) twice, one with conductivity of them medium and one using the conductivity that is perturbed by the chargeability. The apparent (partial) chargeability can be computed as a function of the decaying voltage generated after the current shutdown as:

$$M_a = \frac{1}{\delta\psi_0}\int_{t_i}^{t_{i+1}} \delta\psi_{\mathrm{MN}}(t)dt \tag{22}$$

where $\delta\psi_{\mathrm{MN}}(t)$ is the time dependent decaying voltage recorded between electrodes M and N.

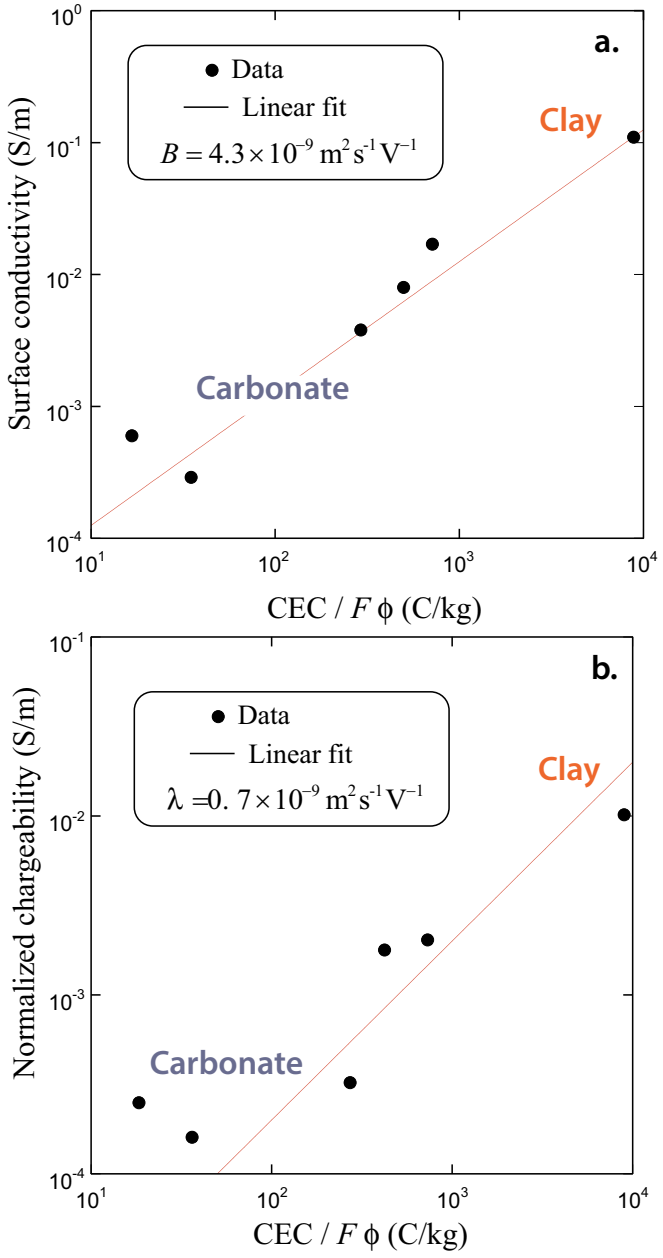

Fig. 7. Normalized chargeability versus CEC. (a) Surface conductivity versus the CEC divided by the tortuosity of the pore space (determined as the product of the formation factor by the porosity). The linear fit is done with $\sigma_S = a$CEC/$F\phi$ with $a = 13 \pm 1 \times 10^{-6}$ in SI units and $r = 0.98$. (b) Normalized chargeability versus CEC/$F\phi$ ($r = 0.97$). The fits are used to determine the value of the mobilities B and λ.

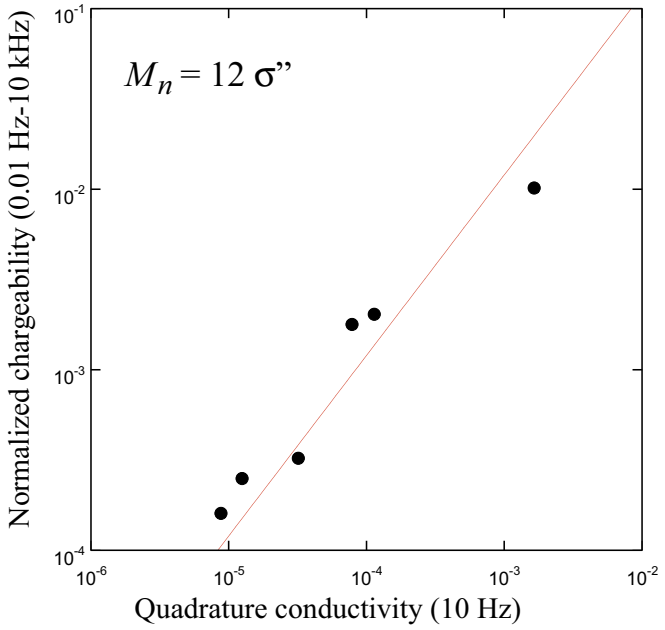

Fig. 8. Normalized chargeability versus quadrature conductivity. In this plot the normalized chargeability is determined between a very low frequency (0.01 Hz) and a high frequency (10 kHz). The quadrature conductivity is determined at the geometric mean frequency of 10 Hz (see Eqs. (6) and (7)). The red plain line corresponds to the best fit used to determine the value of $\alpha = 12$. (For interpretation of the references to colour in this figure legend, the reader is referred to the web version of this article.)

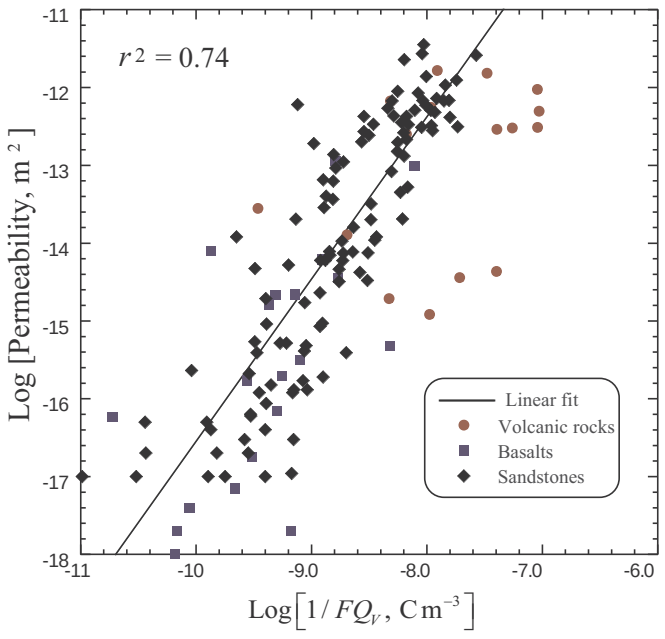

Fig. 9. Permeability as a function of the formation factor F and the volumetric charge density Q_V, which is related to the porosity and the cation exchange capacity. Data from: Niu et al. (2016), Revil et al. (2017a, 2017b), Ghorbani et al. (2018), and Heap et al. (2017), and Sen et al. (1990). The linear fit (least square regression) yields $k = 10^{4.30}(1/FQ_V)^{2.09}$ ($r^2 = 074$).

3.2. Tomography

The tomography of the subsurface here refers to the process through which we seek to recover the physical parameters that give rise to the data that we measure. This is an inverse problem in which the model

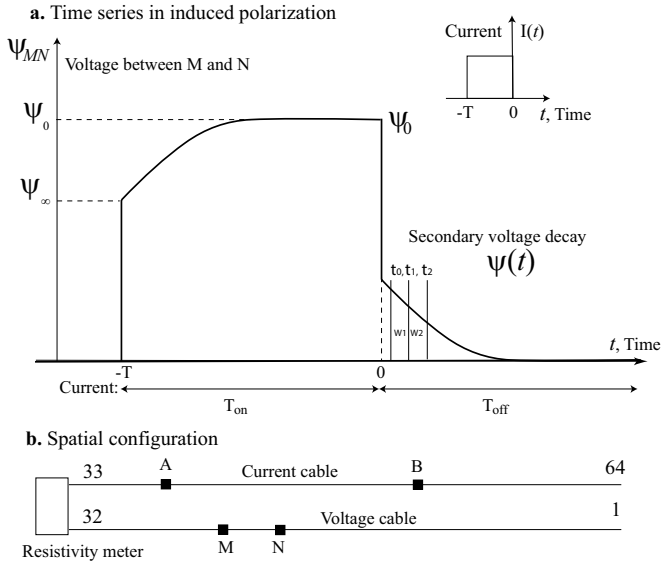

Fig. 10. Time-domain induced polarization data. (a) We inject the current between electrodes A and B (a box signal of period T). The potential difference between the electrodes M and N is the sum of a primary (instantaneous) voltage ψ_∞ and a secondary voltage ψ_0–ψ_∞ for which ψ_0 denotes the steady-state potential. (b) Spatial configuration for a time-domain induced polarization survey. We used two sets of 32 electrodes for the current electrodes and 32 electrodes for the voltage electrodes. These two sets are located on two distinct cables to minimize spurious electromagnetic effects and electrode polarization effects.

vector corresponds to the physical parameters of interest (conductivity and chargeability) discretized over a grid representing a discretization of the subsurface in cells. In our case, the relationship between the data (i.e., the electric potential) and the unknown (i.e., the conductivity and the chargeability) is given by the nonlinear forward operator described in Eq. (14). The idea is to obtain the most optimal parameter set whose computed response matches the observed data and also does exhibit the heterogeneities of the subsurface. In practice, the inverse problem is discretized i.e., the domain of simulation is divided into cells, to each of which we assign a constant value of the physical parameter and the grouping of each these cells gives the global image of the field of the parameter in question. This means that we are not actually dealing with one unknown but with a set of unknowns that may contain several thousands of unknowns or several millions in case of large-scale applications. The difficulty that arises within this context is to obtain a parameter model that has a large number of elements while the amount of data is generally limited and far smaller than the number of unknowns. A common approach employed in the realm of geophysical inversion is to add information that may complete the one provided by the data and also copes with the possible lack of data and the noise it may contain. This strategy is known as regularization (e.g., Tikhonov, 1943). Thus, the inverse problem could be casted into a minimization problem in which, we seek to minimize a misfit function given by:

$$\wp^\alpha = \|W_d(d^{obs} - d^{sim})\|^2 + \alpha\, \|W_m(m - m_{ref})\|^2 \tag{23}$$

where W_d is a diagonal covariance matrix accounting for errors in the data, d^{obs} is the vector of observed data, d^{sim} is the vector of simulated data, W_m is the constraints matrix, α is a positive regularization parameter that serves as a balance or weighting factor for giving different weight to the constraints term or to the data term, m is the discretized physical parameter vector, m_{ref} is the initial a parameter set. The constraints that we impose through the matrix W_m depend on our initial knowledge about the medium. If we are working on gradually variable media without abrupt change in physical properties, smoothing constraints are favored. If we are in the presence of media with discontinuities such as faults or factures, structural constraints are

privileged (e.g., Gallardo and Meju, 2004; Zhou et al., 2014). An efficient and simple way of implementing the smoothing constraints is by choosing the matrix W_m as a combination of the derivative operators that act as smoothing operators on each cell of the inversion mesh. As the inverse problem is nonlinear, it is iteratively solved and during each iteration, the model parameters are updated. In the present paper, we use the popular software Res2Dinv (Loke, 2002) for performing the 2.5 D TDIP inversion of the electrical conductivity and chargeability fields. For more detailed information regarding the inversion process, the reader is invited to refer to (Loke and Barker, 1996a, 1996b; Loke and Dahlin, 2002).

4. Case study

The investigated canal is located in Provence-Alpes-Côte d'Azur region in southern France. The canal is classified A, which means that it is subject to a full technical exam each 10 years. Induced polarization measurements have never been operated on this embankment. The crest of the canal is 4 *m* wide (Fig. 2). Its right bank is built on alluviums of different types including silt, sand, gravel and chipped stones. The left bank is mainly built on materials including limestones, marls, and argilites. This said, due to the topography, the structure of the canal is mainly composed of rockfills on its right bank and is composed of excavation materials on its left bank.

The TDIP measurements were acquired on a portion of the left bank of the canal using a 4-channels ABEM SAS-4000 in July 2019 (Fig. 2). We used two cables as shown in Fig. 10. We performed a 560 *m* long induced polarization profile located at the middle of the crest of the left bank of the canal. This profile was acquired using the roll-along technique which allows for setting up elongated resistivity or IP profiles. Eight IP profiles, each of which is composed of 64 electrodes were concatenated to obtain the long profile (512 electrodes in total were used and the electrodes were moved by set of 16 electrodes to minimize the gaps in the pseudo-section, Fig. 2). The electrodes are separated from each other by a distance of 4 *m* and the injected current amplitude is automatically adapted by the equipment but its minimal amplitude was 20 mA. The voltage decay is recorded on ten 100 ms time windows and after a dead time of 100 ms after cutting off the current to avoid capacitive and inductive effects. The period of the current injection is 1 s.

A total of 1696 apparent resistivities and chargeabilities were acquired. For the acquisition of the induced polarization data, we followed the strategy proposed by Dahlin et al. (2002) for improving the quality of the induced polarization measurements. This technique consists in using for each profile two parallel distinct cables, which means that injection electrodes are laid out along one cable and the measuring electrodes are laid out along the second cable parallel to the other one. The distance between the two cables is 1 m. Although this strategy reduces the depth of investigation, it however has the advantage of avoiding the recording of the noisy current that may corrupt the voltages measured on the same electrodes that have been used both for injecting the current and measuring the voltage after the current has been shut down. Fig. 11 shows an example of the decay curves that we have obtained on the field using this technique. The decaying shape of the curve gives an idea on the good quality of the acquired induced polarization data.

The simulation domain is discretized into 3542 rectangular cells, within each of them the physical parameters of the subsurface are estimated. We used the commercial software Res2DINV (e.g., Loke, 2004) for performing the inversion. We used a smoothing-constrained inversion based on the L2 norm. The inversions of the conductivity and chargeability fields are launched using the means of the apparent resistivity and apparent chargeability as starting models. The inversion process first estimates the conductivity distribution, and then it uses it

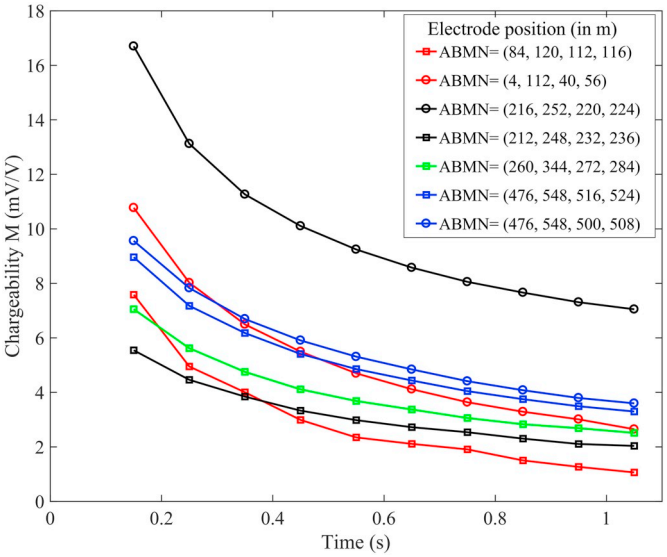

Fig. 11. Apparent chargeability decay curves (expressed in mV/V) for few quadrupoles ABMN. We note the good quality of the measurements showing regular decay for the apparent chargeability with the elapsed time after the shutdown of the primary current.

in the computation of the intrinsic chargeability distribution. The normalized chargeability tomogram is obtained by multiplying the conductivity by the chargeability on each cell of the inversion mesh. Convergence was reached after 5 iterations. Fig. 12a shows the estimated conductivity field which reflects a shallow more resistive zone corresponding to the unsaturated area and deeper more conductive anomalies that represent the fully saturated area. Fig. 12b shows the normalized chargeability field. Higher normalized chargeability anomalies are visible in the deeper areas of the tomograms which coincide with the presence of clayey materials. The shallow less chargeable area corresponds to the carbonates formation. To assess the quality of the inversion results, we report the root means square error (RMSE) for both the conductivity and chargeability fields. The conductivity RMSE is 16%, while the chargeability RSME is 6%. The high RMS error on the conductivity is due to the high input impedance of the ground when the measurements were done in summer 2019 during a heat wave. We could have smooth out the apparent resistivity to reduce the RMS error but we know by experience that such procedure does not change the final result/tomogram. The computed apparent resistivity and chargeability data reproduce the observed data with a good accuracy.

In Fig. 13, we plot the normalized chargeability as a function of the conductivity for both the field and laboratory data. The complete dataset exhibits a first-order linear trend between the two parameters. Low values correspond to the carbonates and high values correspond to clay-rich media. The black plain line corresponds to the expected maximum relationship between the normalized chargeability and conductivity with $R = 0.10$ as discussed in Section 2. Note that the laboratory measurements are performed at full saturation at the in situ pore water conductivity (0.0512 S m^{-1} at 25 °C). The field data are obtained in the vadose zone, so in unsaturated conditions.

The CEC distribution (see Fig. 14b) is high in the clay-rich area with a maximum value close to 40 meq/100 g and a minimum value of 0.8 meq/100 g. This value is on the same order of magnitude than the measurement done in the laboratory for the clayey soil and close to 9 meq/100 g (Table 1). The water content distribution is shown in Fig. 14a. It indicates that the permeable formations are rather dry while the low-permeability formations are rather water-saturated likely

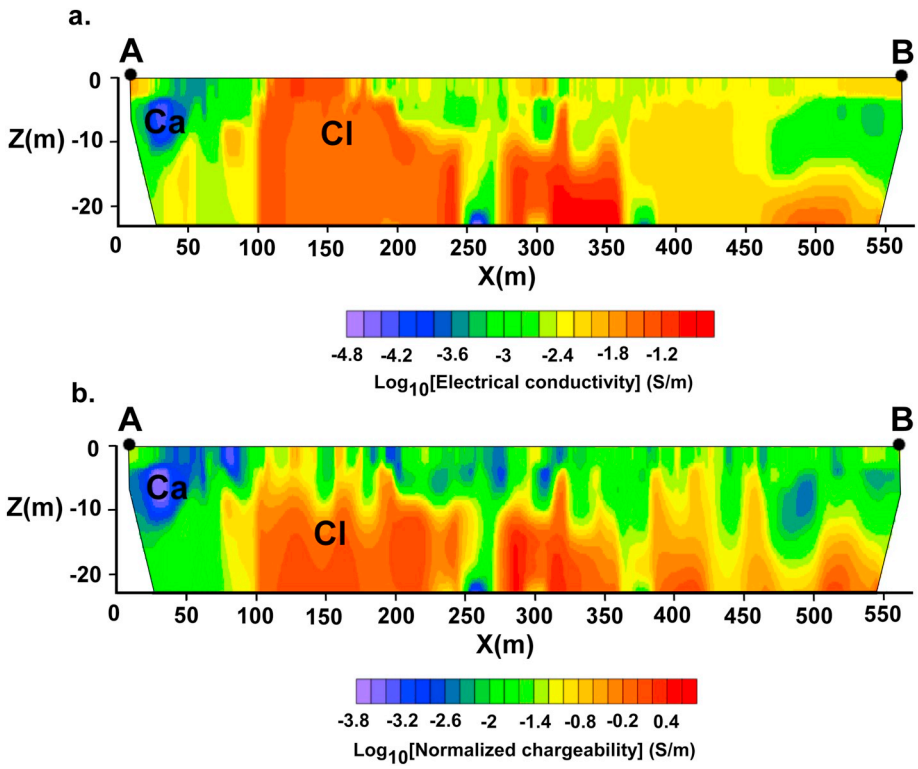

Fig. 12. Induced polarization tomography along the Profile AB (A is located upstream along the canal). (a) Inverted electrical conductivity tomogram. (b) Estimated normalized chargeability tomogram. The carbonate formation is characterized by the low values of the normalized chargeability and electrical conductivity while the clay-rich formation is characterized by high values of the normalized chargeability and electrical conductivity. Ca and Cl correspond to the carbonate and clay rich zones, respectively.

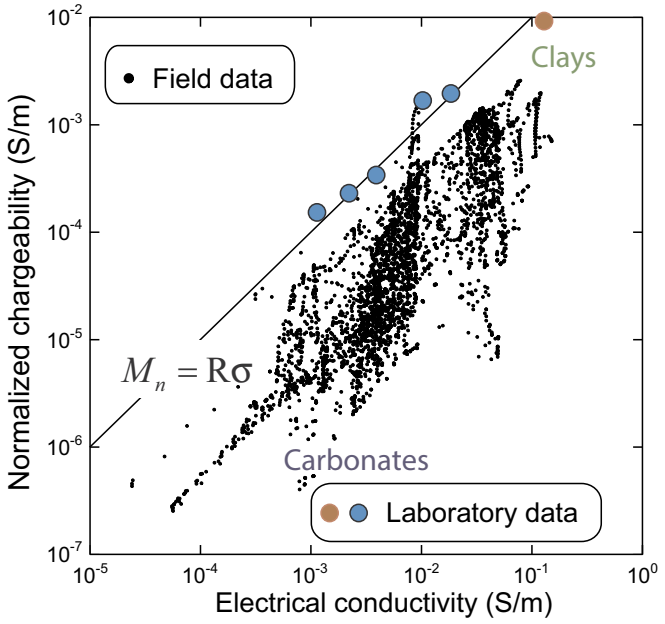

Fig. 13. Normalized chargeability versus electrical conductivity for the field data. Low values correspond to the carbonates and high values correspond to clay-rich media. The black plain line corresponds to the expected maximum relationship between the normalized chargeability and conductivity with $R = 0.10$. Note that the laboratory measurements are performed at full saturation at the in situ pore water conductivity (0.0512 S m^{-1} at 25 °C). The field data are obtained in the vadose zone, so in unsaturated conditions.

because of the high water retention of the clayey materials. By high and low permeability, we mean here the permeability at full water saturation. However, we need to remember that we are here in the vadose zone for which the permeability depends also (and strongly) on the water saturation itself. In Fig. 15, we show the permeability index computed from Eq. (13). This distribution shows a well-defined area (in red) for a high-permeability zone. This high permeability zone is close to the top of the clay-rich zone.

5. Discussion and conclusion

We have conducted a time domain induced polarization survey on an earth dam in Southern France and we have performed spectral Induced polarization in the laboratory as well as petrophysical analyses on core samples collected from the same embankment. Our goal was to investigate the usefulness of the induced polarization method for characterizing the lithology and hydraulic parameters of the structures of earth dams. Indeed, thanks to the development of recent petrophysical models and the development of efficient laboratory equipments, the polarization mechanisms are well understood both at the microscale and macroscale. Through our approach, we are able to image the conductivity, the normalized chargeability, and from these data we can image the cation exchange capacity (CEC), the water content of the dam's structure and its permeability. In terms of lithological discrimination, the tomograms of the normalized chargeability and the CEC clearly show the shallow distribution of carbonates as well as the distribution of the clay-rich materials layer that is located beneath it. The water content distribution is low in the layer corresponding to the unsaturated zone. The petrophysical and spectral induced polarization measurements performed on the six samples are in agreement with the field tomograms, giving values of the measured physical parameters that are in the same range as those imaged by the tomograms. This demonstrates the reliability of our approach and its suitability for the large scale characterization of earth dams.

Next steps will be to test the present approach in highly controlled environments such as big sandbox experiments to test its advantages and limitations.

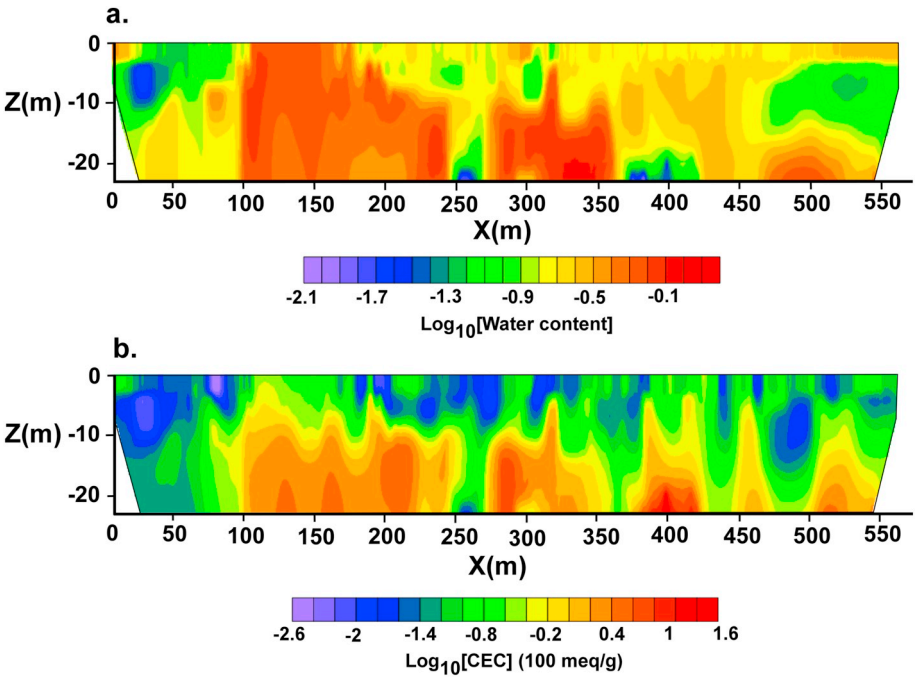

Fig. 14. CEC and pore water content estimations. (a) CEC tomogram. (b) Water content tomogram. Note we are in the vadose zone so the water content in clay materials is expected to be high because of their high retention ability for water.

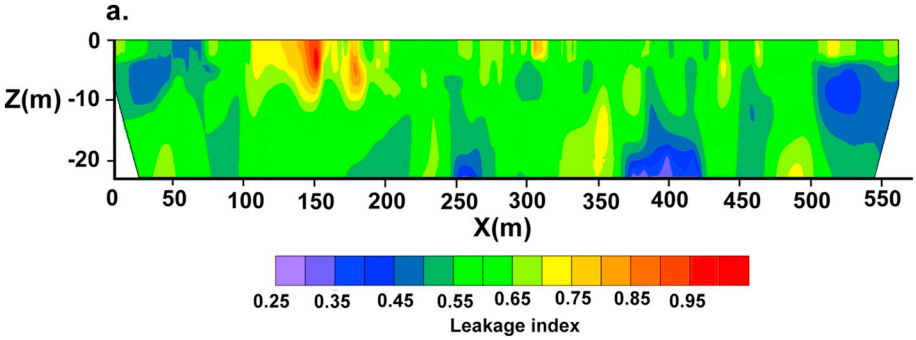

Fig. 15. Permeability index with the red area corresponding to an area of high permeability. (For interpretation of the references to colour in this figure legend, the reader is referred to the web version of this article.)

CRediT authorship contribution statement

A. Soueid Ahmed: Methodology, Writing - original draft, Writing - review & editing, Conceptualization.**A. Revil:**Methodology, Writing - original draft, Writing - review & editing, Conceptualization, Methodology, Data curation, Supervision.**F. Abdulsamad:**Methodology, Writing - original draft, Writing - review & editing, Conceptualization.**B. Steck:**Methodology.**C. Vergniault:** Methodology.**V. Guihard:**Methodology.

Declaration of competing interest

The authors declare that they have no known competing financial interests or personal relationships that could have appeared to influence the work reported in this paper.

Acknowledgments

We thank EDF as well for funding this project in collaboration with the CNRS (Centre National pour la Recherche Scientifique). The postdoc of Abdellahi Soueid Ahmed is funded by EDF through a contract with the CNRS. This work is also supported by the project RESBA ALCOTRA funded by the European Community. We thank the Editor and two Referees for their time and useful comments.

Appendix A. Determination of the CEC and water content

We can rewrite Eqs. (2) and (5) to show explicitly the relationships between the instantaneous conductivity and normalized chargeability as a function of the water content

$$\sigma_\infty \approx \theta^m \sigma_w + \theta^{m-1} \rho_g B \, \mathrm{CEC}, \tag{A1}$$

$$M_n = \theta^{m-1} \rho_g \lambda \, \mathrm{CEC}. \tag{A2}$$

Assuming that $m \approx n$ (i.e., the porosity exponent of the first Archie's law is equal to the saturation exponent of the second Archie's law, an assumption often made in the oil industry when interpreting well-log measurements). Eq. (A2) can be used to express the relationship between the water content and the CEC as,

$$\mathrm{CEC} = \frac{M_n}{\theta^{m-1}\rho_g\lambda}. \tag{A3}$$

Reporting Eq. (A3) in Eq. (A1) yields

$$\sigma_\infty \approx \theta^m\sigma_w + \frac{M_n}{R}, \tag{A4}$$

and $R = \lambda/B$. It follows,

$$\theta = \left[\frac{1}{\sigma_w}\left(\sigma_\infty - \frac{M_n}{R}\right)\right]^{1/m}. \tag{A5}$$

Therefore the water content is determined from the instantaneous conductivity σ_∞ of the porous material, the conductivity of the pore water σ_w, and the normalized chargeability M_n. Then the CEC is determined from Eq. (A3).

References

Abdulsamad, F., Revil, A., Soueid Ahmed, A., Coperey, A., Karaoulis, M., Nicaise, S., Peyras, L., 2019. Induced polarization tomography applied to the detection and the monitoring of leaks in embankments. Eng. Geol. 254, 89–101. https://doi.org/10.1016/j.enggeo.2019.04.001.

Aran, D., Maul, A., Masfaraud, J.-F., 2008. A spectrophotometric measurement of soil cation exchange capacity based on cobaltihexamine chloride absorbance. Compt. Rendus Geosci. 340 (12), 865–871. https://doi.org/10.1016/j.crte.2008.07.015.

Archie, G.E., 1942. The electrical resistivity log as an aid in determining some reservoir characteristics. Trans. AIME 146, 54–62.

Bleil, D.F., 1953. Induced polarization: a method of geophysical prospecting. Geophysics 18, 636–661. https://doi.org/10.1190/1.1437917.

Börner, F.D., Schopper, J.R., Weller, A., 1996. Evaluation of transport and storage properties in the soil and groundwater zone from induced polarization measurements. Geophys. Prospect. 44 (4), 583–601. https://doi.org/10.1111/j.1365-2478.1996.tb00167.x.

Ciesielski, H., Sterckeman, T., Santerne, M., Willery, J.P., 1997. Determination of cation exchange capacity and exchangeable cations in soils by means of cobalt hexamine trichloride. Effects of experimental conditions. Agron. Sci. Prod. Vég. l'Environ. 17 (1), 1–8.

Dahlin, T., Leroux, V., Nissen, J., 2002. Measuring techniques in induced polarization imaging. J. Appl. Geophys. 50, 279–298. https://doi.org/10.1016/S0926-9851(02)00148-9.

Dey, A., Morrison, H.F., 1979. Resistivity modelling for arbitrarily shaped two-dimensional structures. Geophys. Prospect. 27, 106–136. https://doi.org/10.1111/j.1365-2478.1979.tb00961.x.

Fell, R., MacGregor, P., Stapledon, D., 1992. Geotechnical Engineering of Embankment Dams. Balkema, Rotterdam9054101288.

Fell, R., Wan, C.F., Cyganiewicz, J., Foster, M., 2003. Time for development of internal erosion and piping in embankment dams. J. Geotech. Geoenviron. 127, 307–314.

Fransisco, J.M., Fernando, D., Jesús, G., Wenceslao, M., Manuel, L., Lourdes, G., 2018. Identification of leakage and potential areas for internal erosion combining ERT and IP techniques at the Negratín Dam left abutment (Granada, southern Spain). Eng. Geol. 240, 74–80. https://doi.org/10.1016/j.enggeo.2018.04.012.

Gallardo, L.A., Meju, M.A., 2004. Joint two-dimensional DC resistivity and seismic travel time inversion with cross-gradients constraints. J. Geophys. Res. Solid Earth 109. https://doi.org/10.1029/2003JB002716.

Ghorbani, A., Revil, A., Coperey, A., Soueid, Ahmed A., Roque, S., Heap, M.J., Grandis, H., Viveiros, F., 2018. Complex conductivity of volcanic rocks and the geophysical mapping of alteration in volcanoes. J. Volcanol. Geotherm. Res. 357, 106–127. https://doi.org/10.1016/j.jvolgeores.2018.04.014.

Heap, M.J., Kennedy, B.M., Farquharson, J.I., Ashworth, J., Mayer, K., Letham-Brake, M., Siratovich, P., 2017. A multidisciplinary approach to quantify the permeability of the Whakaari/White Island volcanic hydrothermal system (Taupo Volcanic Zone, New Zealand). J. Volcanol. Geotherm. Res. 332, 88–108. https://doi.org/10.1016/j.jvolgeores.2016.12.004.

Himi, M., Casado, I., Sendros, A., Lovera, R., Rivero, L., Casas, A., 2018. Assessing preferential seepage and monitoring mortar injection through an earthen dam settled over a gypsiferous substrate using combined geophysical methods. Eng. Geol. 246, 212–221. https://doi.org/10.1016/j.enggeo.2018.10.002.

Kemna, A., Binley, A., Cassiani, G., Niederleithinger, E., Revil, A., Slater, L., Williams, K.H., Orozco, A.F., Haegel, F.-H., Hoerdt, A., 2012. An overview of the spectral induced polarization method for near-surface applications. Near Surf. Geophys. 10, 453–468. https://doi.org/10.3997/1873-0604.2012027.

Lee, J.Y., Choi, Y.K., Kim, H.S., Yun, S.T., 2005. Hydrologic characteristics of a large rockfill dam: implications for water leakage. Eng. Geol. 80, 43–59. https://doi.org/10.1016/j.enggeo.2005.03.002.

Lesmes, D.P., Frye, K.M., 2001. The influence of pore fluid chemistry on the complex conductivity and induced-polarization response of Berea sandstone. J. Geophys. Res. 106, 4079–4090.

Ling, C., Revil, A., Qi, Y., Abdulsamad, F., Shi, P., Nicaise, S., Peyras, L., 2019. Application of the Mise-à-la-Masse method to detect the bottom leakage of water reservoirs. Eng. Geol. 261, 105272. https://doi.org/10.1016/j.enggeo.2019.105272.

Loke, M., 2002. RES2DINV ver. 3.50. Rapid 2-D Resistivity and IP Inversion Using the Least Square Method.

Loke, M.H., 2004. Tutorial: 2-D and 3-D Electrical Imaging Surveys.

Loke, M., Barker, R., 1996a. Practical techniques for 3D resistivity surveys and data inversion. Geophys. Prospect. 44, 499–523. https://doi.org/10.1111/j.1365-2478.1996.tb00162.x.

Loke, M.H., Barker, R.D., 1996b. Rapid least-squares inversion of apparent resistivity pseudosections by a quasi-Newton method. Geophys. Prospect. 44, 131–152. https://doi.org/10.1111/j.1365-2478.1996.tb00142.x.

Loke, M., Dahlin, T., 2002. A comparison of the Gauss–Newton and quasi-Newton methods in resistivity imaging inversion. J. Appl. Geophys. 49, 149–162. https://doi.org/10.1016/S0926-9851(01)00106-9.

Niu, Q., Revil, A., Saidian, M., 2016. Salinity dependence of the complex surface conductivity of the Portland sandstone. Geophysics 81 (2), D125–D140.

Oldenburg, D.W., Li, Y., 1994. Inversion of induced polarization data. Geophysics 59, 1327–1341. https://doi.org/10.1190/1.1443692.

Panthulu, T.V., Krishnaiah, C., Shirke, J.M., 2001. Detection of seepage paths in earth dams using self-potential and electrical resistivity methods. Eng. Geol. 59, 281–295. https://doi.org/10.1016/S0013-7952(00)00082-X.

Pelton, W.H., Ward, S., Hallof, P., Sill, W., Nelson, P.H., 1978. Mineral discrimination and removal of inductive coupling with multifrequency IP. Geophysics 43, 588–609. https://doi.org/10.1190/1.1440839.

Phan, T.N.T., Louvard, N., Bachiri, S.A., Persello, J., Foissy, A., 2004. Adsorption of zinc on colloidal silica, triple layer modelization and aggregation data. Colloids Surf. A Physicochem. Eng. Asp. 244, 131–140.

Press, W.H., Teukolsky, S.A., Vetterling, W.T., Flannery, B.P., 1992. Numerical Recipes in C++. The Art of Scientific Computing. 2. pp. 1002.

Revil, A., 2012. Spectral induced polarization of shaly sands: Influence of the electrical double layer. Water Resour. Res. 48. https://doi.org/10.1029/2011WR011260.

Revil, A., 2013a. Effective conductivity and permittivity of unsaturated porous materials in the frequency range 1 mHz–1GHz. Water Resour. Res. 49, 306–327. https://doi.org/10.1029/2012WR012700.

Revil, A., 2013b. Effective conductivity and permittivity of unsaturated porous materials in the frequency range 1 mHz–1GHz. Water Resour. Res. 49. https://doi.org/10.1029/2012WR012700.

Revil, A., Florsch, N., 2010. Determination of permeability from spectral induced polarization data in granular media. Geophys. J. Int. 181, 1480–1498. https://doi.org/10.1111/j.1365-246X.2010.04573.x.

Revil, A., Coperey, A., Shao, Z., Florsch, N., Fabricius, I.L., Deng, Y., Delsman, J.R., Pauw, P.S., Karaoulis, M., de Louw, P.G.B., van Baaren, E.S., Dabekaussen, W., Menkovic, A.J., Gunnink, L., 2017a. Complex conductivity of soils. Water Resour. Res. 53 (8), 7121–7147. https://doi.org/10.1002/2017WR020655.

Revil, A., Le Breton, M., Niu, Q., Wallin, E., Haskins, E., Thomas, D.M., 2017b. Induced polarization of volcanic rocks. 2. Influence of pore size and permeability. Geophys. J. Int. 208, 814–825. https://doi.org/10.1093/gji/ggw382.

Rosen, L., Baygents, J., Saville, D., 1993. The interpretation of dielectric response measurements on colloidal dispersions using the dynamic Stern layer model. J. Chem. Phys. 98, 4183–4194. https://doi.org/10.1063/1.465108.

Rozycki, A., Ruiz Fonticiella, J.M., Cuadra, A., 2006. Detection and evaluation of horizontal fractures in earth dams using the self-potential method. Eng. Geol. 82, 145–153. https://doi.org/10.1016/j.enggeo.2005.09.013.

Schlumberger, C., 1920. Study of underground electrical prospecting, Paris. pp. 99.

Scott, J.B.T., Barker, R.D., 2003. Determining pore-troat size in Permo-Triassic sandstones from low-frequency electrical spectroscopy. Geophys. Res. Lett. 30, 1450. https://doi.org/10.1029/2003GL016951.

Seigel, H.O., 1959. Mathematical formulation and type curves for induced polarization. Geophysics 24, 547–565. https://doi.org/10.1190/1.1438625.

Sen, P.N., Straley, C., Kenyon, W.E., Whittingham, M.S., 1990. Surface-to-volume ratio, charge density, nuclear magnetic relaxation, and permeability in clay-bearing

sandstones. Geophysics 55 (1), 61–69.
Slater, L., Lesmes, D., 2002. IP interpretation in environmental investigations. Geophysics 67 (1), 77–88. https://doi.org/10.1190/1.1451353.
Soueid Ahmed, A., Revil, A., Gross, L., 2019. Multiscale induced polarization tomography in hydrogeophysics: a new approach. Adv. Water Resour. 134, 103451. https://doi.org/10.1016/j.advwatres.2019.103451.
Tikhonov, A.N., 1943. On the stability of inverse problems. In: Dokl. Akad. Nauk SSSR, pp. 195–198.
Van Voorhis, G.D., P. Nelson, H., Drake, T.L., 1973. Complex resistivity spectra of porphyry copper mineralization. Geophysics 38 (1), 49–60. https://doi.org/10.1190/1.1440333.
Weller, A., Nordsiek, S., Debschütz, W., 2010. Estimating permeability of sandstone samples by nuclear magnetic resonance and spectral-induced polarization. Geophysics 75 (6), E215–E226. https://doi.org/10.1190/1.33507304.
Weller, A., Slater, L., Nordsiek, S., 2013. On the relationship between induced polarization and surface conductivity: implications for petrophysical interpretation of electrical measurements. Geophysics 78, D315–D325. https://doi.org/10.1190/geo2013-0076.1.
Zhou, J., Revil, A., Karaoulis, M., Hale, D., Doetsch, J., Cuttler, S., 2014. Image-guided inversion of electrical resistivity data. Geophys. J. Int. 197, 292–309. https://doi.org/10.1093/gji/ggu001.
Zimmermann, E., Kemna, A., Berwix, J., Glaas, W., Münch, H.M., Huisman, J.A., 2008. A high-accuracy impedance spectrometer for measuring sediments with low polarizability. Meas. Sci. Technol. 19 (10), 105603. https://doi.org/10.1088/0957-0233/19/10/105603.
Zonge, K.L., Wynn, J.C., 1975. Recent advances and applications in complex resistivity measurements. Geophysics 40, 851–864. https://doi.org/10.1190/1.1440572.